Applied Physics Letters

RESEARCH ARTICLE | AUGUST 20 2024

Mode-dependent scaling of nonlinearity and linear dynamic range in a NEMS resonator

M. Ma ; N. Welles ; O. Svitelskiy ; C. Yanik ; I. I. Kaya ; M. S. Hanay ; M. R. Paul ; K. L. Ekinci

Appl. Phys. Lett. 125, 083505 (2024)
https://doi.org/10.1063/5.0215566

AIP Publishing

Applied Physics Letters ARTICLE pubs.aip.org/aip/apl

Mode-dependent scaling of nonlinearity and linear dynamic range in a NEMS resonator

Cite as: Appl. Phys. Lett. **125**, 083505 (2024); doi: 10.1063/5.0215566
Submitted: 24 April 2024 · Accepted: 8 August 2024 ·
Published Online: 20 August 2024

View Online Export Citation CrossMark

M. Ma,[1] N. Welles,[2] O. Svitelskiy,[3] C. Yanik,[4] I. I. Kaya,[4,5] M. S. Hanay,[6,7] M. R. Paul,[2] and K. L. Ekinci[1,a)]

AFFILIATIONS

[1]Department of Mechanical Engineering, Division of Materials Science and Engineering, and the Photonics Center, Boston University, Boston, Massachusetts 02215, USA
[2]Department of Mechanical Engineering, Virginia Tech, Blacksburg, Virginia 24061, USA
[3]Department of Physics, Gordon College, Wenham, Massachusetts 01984, USA
[4]SUNUM, Nanotechnology Research and Application Center, Sabanci University, Istanbul 34956, Turkey
[5]Faculty of Engineering and Natural Sciences, Sabanci University, Istanbul 34956, Turkey
[6]Department of Mechanical Engineering, Bilkent University, Ankara 06800, Turkey
[7]National Nanotechnology Research Center (UNAM), Bilkent University, Ankara 06800, Turkey

[a)]**Author to whom correspondence should be addressed:** ekinci@bu.edu

ABSTRACT

Even a relatively weak drive force is enough to push a typical nanomechanical resonator into the nonlinear regime. Consequently, nonlinearities are widespread in nanomechanics and determine the critical characteristics of nanoelectromechanical systems' (NEMSs) resonators. A thorough understanding of the nonlinear dynamics of higher eigenmodes of NEMS resonators would be beneficial for progress, given their use in applications and fundamental studies. Here, we characterize the nonlinearity and the linear dynamic range (LDR) of each eigenmode of two nanomechanical beam resonators with different intrinsic tension values up to eigenmode $n = 11$. We find that the modal Duffing constant increases as n^4, while the critical amplitude for the onset of nonlinearity decreases as $1/n$. The LDR, determined from the ratio of the critical amplitude to the thermal noise amplitude, increases weakly with n. Our findings are consistent with our theory treating the beam as a string, with the nonlinearity emerging from stretching at high amplitudes. These scaling laws, observed in experiments and validated theoretically, can be leveraged for pushing the limits of NEMS-based sensing even further.

Over the past decade, the sensitivities attainable by nanoelectromechanical systems (NEMS) have steadily approached fundamental limits.[1–6] In a typical NEMS sensing application, one drives the NEMS resonator at one of its resonances and looks for changes in its resonance frequency or amplitude due to a prescribed interaction with the environment. The highest sensitivity is attained when the mode is driven to the largest amplitude possible, and its oscillations are detected by the lowest-noise motion transducer available.[7] All these considerations are captured in a widely used and intuitive formula that provides the minimum detectable frequency shift (i.e., rms frequency noise) δf for a NEMS-based resonant sensor,[8]

$$\delta f \approx \frac{f}{2Q}\, 10^{-\frac{\mathrm{LDR}}{20}}. \tag{1}$$

Here, f and Q are the resonance frequency and the quality factor of the NEMS mode, respectively, and linear dynamic range (LDR) of the mode (in units of dB) is defined as[9]

$$\mathrm{LDR} = 20 \log\left(\frac{0.745 z_c}{z_N}\right), \tag{2}$$

where z_c is the so-called critical amplitude (rms) for the onset of nonlinearity of the mode: more precisely, the frequency-response curve for the mode first attains infinite slope at z_c as the drive force is increased; z_N is the rms noise amplitude within the measurement bandwidth. The numerical factor quantifies the 1 dB compression that occurs when the signal is 1 dB below the expected linear response. It is immediately evident from Eqs. (1) and (2) that, to maximize the signal-to-

noise ratio (SNR) in *linear* NEMS operation, the NEMS resonator must be driven to the cusp of nonlinearity.[10,11] A formula similar to Eq. (1) exists for amplitude detection.[12]

The aforementioned discussion suggests that it is important to understand and characterize nonlinearities in NEMS. In particular, the LDR—and, consequently, the onset of nonlinearity and the amplitude of thermal fluctuations—of a NEMS resonator is one of the most essential device parameters for sensing. As an NEMS resonator is uniformly scaled down, its spring constant tends to become smaller, and thermal fluctuations become more prominent.[13] This indicates that the LDR will shrink from the bottom end. Experiments on different structures[9,14–16] have shown that the amplitude for the onset of nonlinearity becomes progressively smaller for smaller structures, suggesting that the top end of the LDR also gets diminished. In other words, as NEMS gets miniaturized, the LDR tends to keep shrinking,[17,18] leading to next-generation devices that practically have no linear regime.[19,20]

The quintessential NEMS resonator, in which intrinsic nonlinearities have been carefully explored, is a doubly clamped nanomechanical beam vibrating in its fundamental mode.[9,18,21,22] The most commonly studied intrinsic nonlinearity emerges through tension that develops as the beam stretches at high amplitudes. Analytical description of this system starting with the elastic beam equation leads to the Duffing equation for the fundamental mode.[23–26] A quadratic term may also emerge if a broken symmetry exists in the system.[17,27,28] The analytical theory accurately predicts both the Duffing constant and the onset of nonlinearity for the fundamental mode of NEMS beams made out of different materials[21,29–31] and with different intrinsic tension levels.[18,32–34] This consequently allows for a reasonable estimate of the LDR.[9,17]

As the NEMS sensor work progresses, it has become more common to employ higher modes or multiple modes in applications.[35,36] With some notable exceptions,[23,37–39] there has not been much insight into the nonlinearities and LDR of high modes. In this manuscript, we provide a theoretical framework and experimental measurements that describe how intrinsic nonlinearity scales with eigenmode number n in a NEMS resonator. We also measure the thermal noise of each eigenmode and elucidate the n dependence of the LDR. We conclude that the useful LDR increases with increasing intrinsic tension in the device and n, albeit slowly.

We begin with the Euler-Bernoulli beam equation with an intrinsic tension term. We also include a nonlinear tension term resulting from the stretching of the beam that occurs for large amplitude oscillations. This can be expressed as[9,21,23]

$$\rho A\frac{\partial^2 Z(x,t)}{\partial t^2}+EI\frac{\partial^4 Z(x,t)}{\partial x^4}-\left[F_T+\frac{EA}{2l}\int_0^l\left(\frac{\partial Z}{\partial x}\right)^2 dx\right]\frac{\partial^2 Z(x,t)}{\partial x^2}=0. \tag{3}$$

Here, $Z(x, t)$ is the out-of-plane flexural displacement of the beam at axial position x and time t [Fig. 1(a)]; $l \times w \times h$ are the nominal dimensions along x, y, and z, $A = wh$ is the cross-sectional area, and $I = wh^3/12$ is the area moment of inertia of the beam; the beam has Young's modulus E and density ρ. The first term in Eq. (3) is the inertial term, the second term is the rigidity term, and the third term is the tension term. The first component of the tension term in the square brackets is the intrinsic tension F_T, and the second term corresponds to the additional tension due to stretching. Ignoring the nonlinear term for a moment and non-dimensionalizing Eq. (3), we obtain the nondimensional tension parameter,[40,41]

$$U=\frac{F_T}{2EI/l^2}, \tag{4}$$

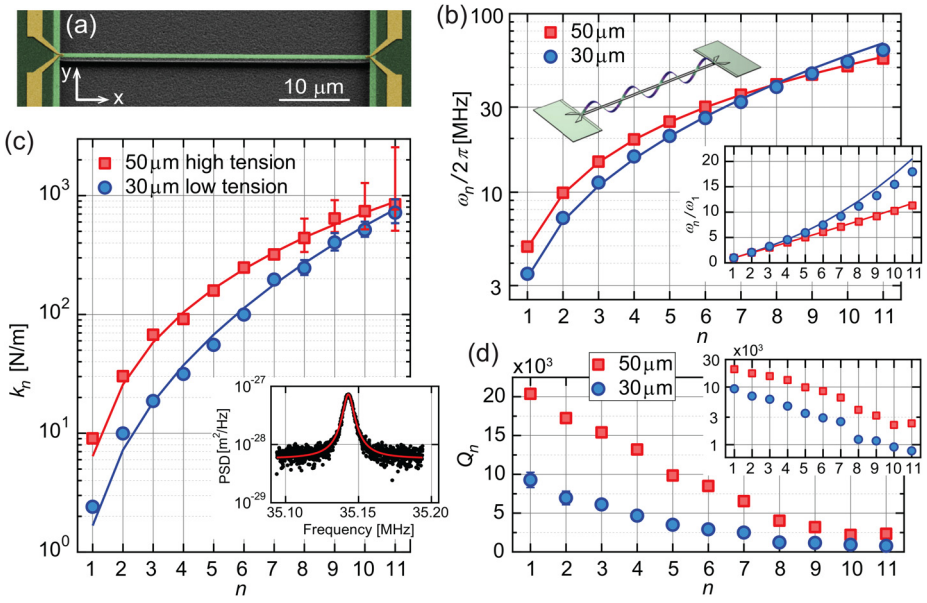

FIG. 1. (a) SEM image of a NEMS doubly clamped beam with thin-film gold nanoresistors around both anchors. (b) Experimental and theoretical eigenfrequencies $\omega_n/2\pi$ shown on a semilogarithmic plot. The upper inset is a numerical simulation of the seventh eigenmode; the lower inset shows ω_n/ω_1 on a linear plot. (c) Experimental and theoretical spring constants k_n shown on a semilogarithmic plot. Error bars are smaller than the symbols unless explicitly shown. Inset shows the PSD of the thermal fluctuations of the seventh mode with a Lorentzian fit to the peak. (d) Experimental quality factors Q_n decrease as a function of n. Inset shows the same data on a semilogarithmic plot.

which represents the ratio of the axial load on the beam to its rigidity. The system approaches an Euler-Bernoulli beam for $U \ll 1$ and a string for $U \gg 1$.

In the limit $U \gg 1$, we neglect the bending term to obtain the (nonlinear) string equation,

$$\rho A \frac{\partial^2 Z(x,t)}{\partial t^2} - \left[F_T + \frac{EA}{2l} \int_0^l \left(\frac{\partial Z}{\partial x} \right)^2 dx \right] \frac{\partial^2 Z(x,t)}{\partial x^2} = 0, \quad (5)$$

with boundary conditions $Z(0,t) = Z(l,t) = 0$ and eigenfunctions $\phi_n(x) = \sin\left(\frac{n\pi x}{l}\right)$. Expanding the solution $Z(x, t)$ in terms of the orthogonal $\phi_n(x)$ and integrating over the length of the beam[9,23] yields a Duffing equation for the time dependent amplitude $z_n(t)$ of the different modes. Including a lumped drive force of amplitude F_n at frequency $\omega \approx \omega_n$ as well as a small phenomenological damping term, we arrive at[9,21,23]

$$\ddot{z}_n + \frac{\omega_n}{Q_n} \dot{z}_n + \omega_n^2 z_n + \alpha_n z_n^3 = \frac{F_n}{m_n} \cos \omega t. \quad (6)$$

This eigenfunction expansion yields the usual expression for the eigenfrequency $\omega_n = \frac{n\pi}{l} \sqrt{\frac{F_T}{\rho A}}$; the modal spring constant (referred to an antinode[13]) and the modal mass can be found as $k_n = \frac{\pi^2 F_T}{2l} n^2$ and $m_n = k_n/\omega_n^2 = \frac{\rho l A}{2}$, respectively.[40,42] Most importantly, the modal Duffing constant α_n emerges as[23]

$$\alpha_n = \left(\frac{E\pi^4}{4\rho l^4} \right) n^4. \quad (7)$$

With the aforementioned choice of the eigenfunctions, $z_n(t)$ corresponds to the actual (peak) displacement of the string at its antinodes. We note that, even for large U, the string approximation is expected to break down for large n, where bending becomes important.

Returning to Eq. (6), standard steps[9,21,23–25] lead to an expression for the frequency of the peak $\omega_{p,n}$ as a function of the peak amplitude $z_{p,n}$ and other modal parameters,

$$\omega_{p,n} = \omega_n + \frac{3}{8} \left(\frac{z_{p,n}^2}{\omega_n} \right) \alpha_n. \quad (8)$$

Equation (8) is parabolic in $z_{p,n}$ and describes the backbone curve,[21,24] which follows the peak as the amplitude increases.

The critical amplitude $z_{c,n}$ can be determined from Eq. (6) by performing a multiple-scale analysis,[9,24] which yields

$$z_{c,n} = \sqrt{\frac{8\sqrt{3}}{9} \frac{\omega_n^2}{Q_n \alpha_n}}. \quad (9)$$

Substituting for the string values of ω_n and α_n in Eq. (9) and realizing that $U = \left(\frac{l}{h}\right)^2 \left(\frac{6F_T}{EA}\right)$, we arrive at[23]

$$z_{c,n} = \left(\frac{4h}{3^{5/4}\pi} \sqrt{\frac{U}{Q_n}} \right) \frac{1}{n}. \quad (10)$$

The tension parameter U, when considered in Eq. (10), represents the ratio of the intrinsic tension to the elasticity induced tension due to the stretching of the beam.

Our experimental study is based on two silicon nitride (SiN) NEMS doubly clamped beam resonators with different intrinsic tension values. These two resonators are fabricated on two different wafers, one with higher stress than the other. A colored scanning electron microscope (SEM) image of the high-tension NEMS beam is shown in Fig. 1(a). Here, the beam lies along the x axis, and out-of-plane vibrations are actuated in the z direction. The nominal dimensions of the beam are $l \times w \times h \approx 50\ \mu\text{m} \times 900\ \text{nm} \times 100\ \text{nm}$. The suspended region is shown in bright green and is clamped to the substrate underneath on either side. Gold nanoresistors are patterned on top of the beam near the clamps for electrothermal actuation. Nanoresistors have a width of 120 nm and a thickness of 135 nm. All dimensions of the low-tension beam are the same, except the nanoresistor thickness is 60 nm and $l \approx 30\ \mu\text{m}$. To measure linear and nonlinear parameters of each device, we apply a sinusoidal current to the electrothermal actuators[43] and sweep the frequency from low to high around each eigenfrequency. We detect the NEMS motion interferometrically[43] at the forcing frequency using a lock-in amplifier. By gradually increasing the actuation current, we drive each eigenmode from its linear to nonlinear regime. For each eigenmode, both linear and nonlinear measurements are taken at an antinode closest to the center of the beam. All the experiments are performed in a high vacuum chamber.

Electrothermal actuation is based on Joule heating of the beam around the nanoresistor by an input current.[44] Coupled with the piezoresistance[45] and the temperature-dependent resistivity of the gold nanoresistor, Joule heating can result in mechanical forces and responses at the harmonics of the drive frequency. The lock-in amplifier filters out the higher harmonics, and the mixed down signal components are estimated to be negligible. We have also estimated the nonlinearity of the optical interferometer and found it to be a small but observable source of extrinsic nonlinearity. Finally, nonlinear dissipation is not appreciable in our system (see the supplementary material for details).

We first measure the linear modal parameters of the NEMS beams [Figs. 1(b)–1(d)], including the eigenfrequencies $\omega_n/2\pi$, spring constants k_n, and quality factors Q_n and compute the intrinsic tensions F_T. Figure 1(b) shows $\omega_n/2\pi$ as a function of mode number n in a semilogarithmic plot. Here, the red and blue symbols correspond to the experimental values for the frequencies of the 50 and 30-μm beams, respectively, and the continuous lines correspond to the values computed using tensioned beam theory.[13,40,41] The lower inset shows the normalized frequencies, ω_n/ω_1, on a linear plot and reveals a strong string-like behavior for the 50-μm beam. We find F_T by matching analytical eigenfrequencies $\omega_n/2\pi$ with experiments. For material properties of SiN, we use a Young's modulus of $E = 250\ \text{GPa}$,[46,47] a Poisson's ratio of $\nu = 0.23$, and a mass density of $\rho = 3000\ \text{kg/m}^3$. We find $F_T = 63.5\ \mu\text{N}$ for the 50-μm beam and $F_T = 8.9\ \mu\text{N}$ for the 30-μm beam. The respective U values for the two beams are 4233 and 214. The upper inset in Fig. 1(b) shows the displacement profile for a typical eigenmode, the seventh eigenmode for the 50-μm beam.

Figure 1(c) shows k_n as a function of n in a semilogarithmic plot. To find the experimental k_n, we measure the power spectral density (PSD) of thermal fluctuations for each mode at a modal antinode closest to the center of the beam. We first find the mean-squared fluctuation amplitude by numerically integrating the modal PSD, we then calculate the spring constants from the equipartition of energy.[13] A

representative PSD for the seventh eigenmode of the 50-μm beam is shown in the inset, where the continuous line is a Lorentzian fit to the peak. The continuous lines in the main figure are found from tensioned beam theory using mechanical properties of the beam and F_T.[13,40] Finally, Fig. 1(d) shows the experimental quality factors Q_n, which are determined from linear time-domain ring-downs and frequency-domain Lorentzian fits[45] to the resonator response (see the supplementary material for details). The inset shows the same data on a semilogarithmic plot. Q_n decreases monotonically with increasing mode number n. The observed decrease in Q_n as a function of n is consistent with dissipation dilution,[48–51] and our overall dissipation is likely dominated by the gold film near the anchors.[46]

Next, we show how to extract the nonlinear Duffing constant α_n and the critical amplitude $z_{c,n}$ from a measurement of the NEMS modal response as a function of frequency. Figure 2(a) shows the sixth mode resonance of the 50-μm beam for different rms drive current levels using a logarithmic y axis. The first four response curves at the lowest drive levels are linear. With increasing drive power, the response exhibits nonlinear stiffening: the frequency of the peak increases with the drive, and, at the largest drives, the response makes a downward jump as the response is no longer a singled-valued function of frequency.[24,25] We extract α_n by fitting experimental $z_{p,n}$ values at larger drives to Eq. (8).

Modal α_n values for both beams are shown as a function of $\omega_n/2\pi$ in Fig. 2(b). The y-axis is logarithmic and has units of $\mathrm{MHz}^2/\mathrm{nm}^2$ to yield reasonable numerical values. The inset is a double-logarithmic plot of α_n vs n. The slope reveals that $\alpha_n \propto n^4$. The continuous lines are from theory and are discussed later. All experimentally measured α_n along with linear modal parameters is listed in Table I.

Figure 2(c) (symbols) shows experimental critical amplitudes $z_{c,n}$ as a function of frequency computed from the corresponding α_n using Eq. (9). In the inset, we remove the Q_n dependence of the data by plotting $z_{c,n}\sqrt{Q_n}$ as a function of n in a double-logarithmic plot. The data scale as $z_{c,n}\sqrt{Q_n} \propto \frac{1}{n}$. The continuous theory lines are also discussed later. The $z_{c,n}$ values can also be determined from the modal response curve by finding the first point with infinite slope. These values agree with the $z_{c,n}$ values found using Eq. (9) to within ~10%.

For both beams $U \gg 1$, and it seems reasonable to use the string approximation, i.e., Eqs. (7) and (10), in order to determine the theoretical values for α_n and $z_{c,n}$. To calculate the theoretical curves in Figs. 2(b) and 2(c), we use the nominal dimensions of the beams, mechanical properties of SiN, and experimental values for U and Q_n in Eqs. (7) and (10), respectively. The use of experimentally measured Q_n in Eq. (10) results in the non-smooth theoretical curves in Fig. 2(c). The agreement between experimental and theoretical α_n in Fig. 2(b) is very good for both beams. In Fig. 2(c), the experimental $z_{c,n}$ data deviate from theory for the 30-μm beam at some of the large n values. The reason for this can be traced to the string approximation and its neglect of bending contributions, which become increasingly important at larger n. Equation (9) indicates that any errors in ω_n will be propagated to $z_{c,n}$. Indeed, Fig. 1(b), inset, shows that ω_n for the 30-μm beam deviates from the string frequencies (continuous red curve) for high n.

Finally, we discuss the LDR of these nanomechanical resonators. We modify Eq. (2) to redefine the LDR of mode n as

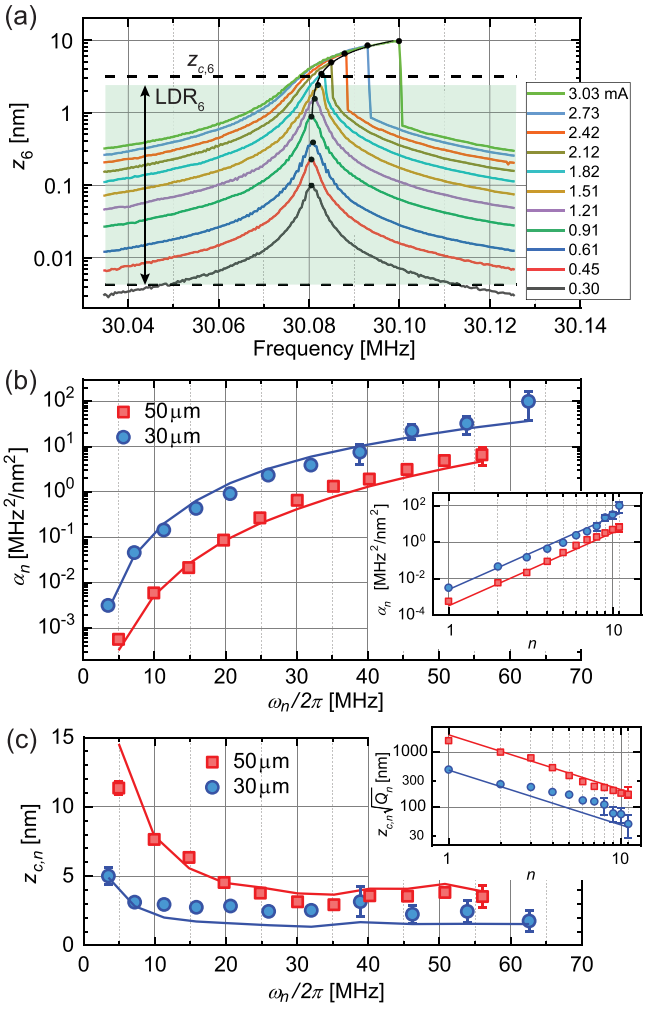

FIG. 2. (a) Frequency-response curves (peak) of the sixth mode of the 50-μm beam for different drive current values (rms). The upper dashed line shows the critical amplitude $z_{c,6}$. The lower dashed line is the rms thermal amplitude $\sqrt{k_BT/k_6}$. The green-shaded area corresponds to the LDR. The Duffing constant α_6 is extracted from a parabolic fit to the backbone curve. (b) Duffing constants α_n as a function of eigenfrequency shown on a semilogarithmic plot. Inset shows α_n as a function of n on a double-logarithmic plot, revealing the trend $\alpha_n \propto n^4$. (c) Critical amplitudes $z_{c,n}$ (peak) as a function of eigenfrequency plotted on linear axes. The theoretical curves are non-smooth due to experimental Q_n. Inset shows $z_{c,n}\sqrt{Q_n}$ as a function of n on a double-logarithmic plot, revealing the trend $z_{c,n}\sqrt{Q_n} \propto 1/n$.

$$\mathrm{LDR}_n = 20\,\log\left(\frac{0.745 z_{c,n}^{(rms)}}{\sqrt{k_BT/k_n}}\right), \tag{11}$$

where the entire noise bandwidth is taken as the detection bandwidth. Equation (11) gives the value of LDR$_n$ referred to an antinode. Returning to Fig. 2(a), the dashed line on the bottom shows the rms thermal amplitude, $\sqrt{k_BT/k_6}$. The modal critical amplitude $z_{c,6}$ is indicated by the upper dashed line, which corresponds to the first displacement amplitude with infinite slope.[24,25] The green-shaded area corresponds to the LDR, with the upper end of the LDR slightly below $z_{c,6}$.

TABLE I. Experimental parameters for the first 11 modes of two NEMS resonators.

	$l \times w \times h = 50\,\mu\text{m} \times 900\,\text{nm} \times 100\,\text{nm}$, $U = 4233$				$l \times w \times h = 30\,\mu\text{m} \times 900\,\text{nm} \times 100\,\text{nm}$, $U = 214$			
Mode	$\omega_n/2\pi$ (MHz)	Q_n	k_n (N/m)	α_n (MHz^2/nm^2)	$\omega_n/2\pi$ (MHz)	Q_n	k_n (N/m)	α_n (MHz^2/nm^2)
1	4.954	2.0×10^4	9.05	5.69×10^{-4}	3.488	9.3×10^3	2.41	3.18×10^{-3}
2	9.927	1.7×10^4	30.2	5.95×10^{-3}	7.169	7.0×10^3	9.96	4.62×10^{-2}
3	14.83	1.5×10^4	67.5	2.15×10^{-2}	11.32	6.1×10^3	18.7	1.46×10^{-1}
4	19.74	1.3×10^4	91.5	8.71×10^{-2}	15.85	4.7×10^3	31.5	4.35×10^{-1}
5	24.83	9.8×10^3	159	2.68×10^{-1}	20.66	3.5×10^3	55.5	9.21×10^{-1}
6	30.08	8.5×10^3	248	6.55×10^{-1}	26.01	2.9×10^3	99.7	2.35
7	35.15	6.5×10^3	320	1.33	32.00	2.5×10^3	196	3.91
8	40.22	4.0×10^3	440	1.92	38.89	1.2×10^3	246	7.54
9	45.52	3.2×10^3	642	3.13	46.21	1.2×10^3	403	2.23×10^1
10	50.78	2.2×10^3	739	4.90	53.92	9.1×10^2	516	3.23×10^1
11	56.06	2.3×10^3	845	6.58	62.60	7.8×10^2	719	9.91×10^1

We compute the experimental LDR_n using experimental values for $z_{c,n}$ [symbols in Fig. 2(c)] and k_n [symbols in Fig. 1(c)]. For the theoretical curves, we use the theoretical $z_{c,n}$ [Eq. (10)], in which U and Q_n are from experiments and theoretical k_n [continuous lines in Fig. 1(c)]. Figure 3(a) shows the experimental and theoretical LDR_n as a function of n for the first 11 modes of the two NEMS resonators. Note, again, that the theoretical curve is non-smooth due to the experimentally measured Q_n values. Both experimental and theoretical LDR show a weak dependence on n.

To better understand the dependence of LDR on physical parameters, we analyze the data in Fig. 3(a) based on Eqs. (10) and (11). We notice that, for the string approximation, the data should only be a function of $\frac{\mathcal{C}}{n}\sqrt{\frac{Uk_n}{Q_n}}$, where $\mathcal{C} \approx \frac{0.24h}{\sqrt{k_B T}}$ is the same constant for both beams. This suggests that all data can be plotted as a function of $\frac{\mathcal{C}}{n}\sqrt{\frac{Uk_n}{Q_n}}$. To determine the new x coordinate for each data point in Fig. 3(a), we compute the corresponding value of $\frac{\mathcal{C}}{n}\sqrt{\frac{Uk_n}{Q_n}}$ based on all the experimental values. We then plot the data point against this x value. The result is plotted in Fig. 3(b). The theory curve is the smooth function $20\log\left(\frac{\mathcal{C}}{n}\sqrt{\frac{Uk_n}{Q_n}}\right)$. The inset shows the same data using a logarithmic x axis and reveals a slope of 1. The agreement between experimental and theoretical LDR for the 50-μm beam is excellent, while the theory underpredicts experimental LDR of the 30-μm beam. The arrows indicate the direction of increasing n for the experimental data.

At a first glance, LDR in Fig. 3(a) increases with n and U. However, k_n and Q_n both depend on U and n. More insight can be gained into the trends by turning to the $U \gg 1$ limit. To this end, we use the string k_n expressed in terms of U as $k_n \approx \frac{\pi^2 UEI}{l^3} n^2$ to find $\text{LDR}_n \approx 20\log\left(0.8h\sqrt{\frac{EI}{l^3 k_B T}}\right) + 20\log\left(\frac{U}{\sqrt{Q_n}}\right)$, both referred to an antinode. For a given string, LDR_n increases with increasing U because $z_{c,n}$ grows and the thermal fluctuation amplitude decreases with U—extending the LDR on both ends. In the string approximation, LDR_n does not explicitly depend upon n but only through Q_n. Intrinsic (*in vacuo*) Q_n tends to decrease[45,50,52] with n, whereas fluidic Q_n may increase[13,53] with n. Comparison between different structures made of different materials is also possible using our formulas and requires knowledge of E in addition to nominal dimensions, U and Q_n.

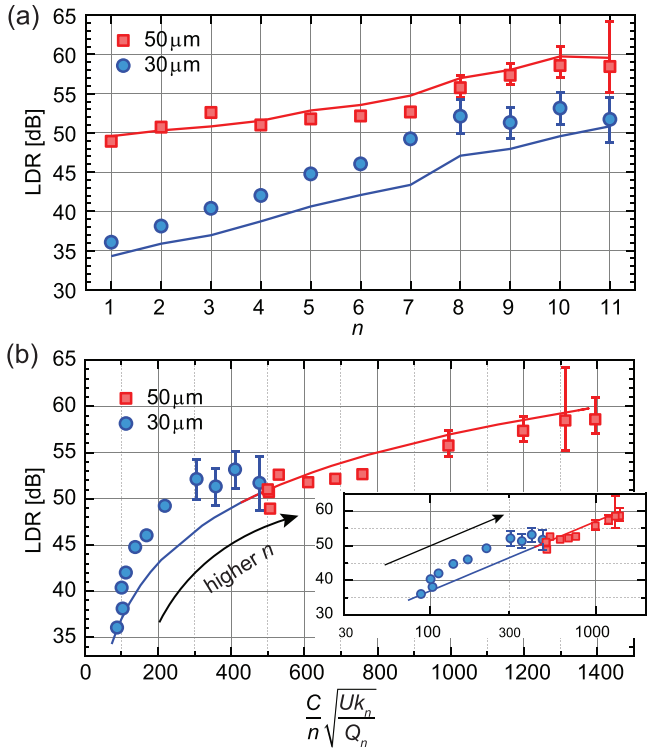

FIG. 3. (a) Experimental and theoretical LDR for 11 eigenmodes of two NEMS resonators computed using Eq. (11). The theoretical curves are non-smooth due to experimental Q_n. (b) Collapsed LDR data. Inset shows the same data on a double-logarithmic plot, revealing a slope of 1.

Our aim here has been to uncover the scaling of α_n, $z_{c,n}$, and LDR_n across eigenmodes in a nanomechanical resonator. To this end, we have formulated our theory based on the string equation [Eq. (5)], which yielded insightful closed-form analytical expressions. We attribute the disagreements between theory and experiment for our lower tension beam to the string approximation and will resolve this in future work by employing the tensioned beam theory. Finally, the frequency resolution and, in particular, mass sensitivity of our NEMS resonators should increase with n, given that LDR increases but the active mass tends to stay unchanged with n.

See the supplementary material for details of computing the experimental values of Q_n and F_T, the theoretical values for k_n and ω_n as well as the error sources in the system. Error sources include intermodal force coupling, transduction nonlinearities, thermally induced frequency shifts, and nonlinear damping.

We acknowledge support from the US NSF (Nos. CMMI 2001403, CMMI 1934271, CMMI 2001559, and CMMI 1934370). M. Ma acknowledges support from Boston University Nanotechnology Innovation Center BUnano Cross-Disciplinary Fellowship. We thank H. Gress for the SEM image of the NEMS device.

AUTHOR DECLARATIONS

Conflict of Interest

The authors have no conflicts to disclose.

Author Contributions

M. Ma: Conceptualization (equal); Data curation (lead); Investigation (equal); Methodology (equal); Validation (equal); Writing – original draft (equal); Writing – review & editing (equal). **N. Welles:** Data curation (equal); Formal analysis (equal); Investigation (equal); Methodology (equal). **O. Svitelskiy:** Formal analysis (equal); Investigation (supporting); Writing – review & editing (supporting). **C. Yanik:** Resources (equal). **I. I. Kaya:** Resources (equal). **M. S. Hanay:** Resources (equal). **M. R. Paul:** Conceptualization (equal); Formal analysis (equal); Methodology (equal); Writing – review & editing (supporting). **K. L. Ekinci:** Conceptualization (equal); Formal analysis (equal); Funding acquisition (equal); Investigation (equal); Methodology (equal); Supervision (lead); Writing – original draft (equal); Writing – review & editing (equal).

DATA AVAILABILITY

The data that support the findings of this study are available from the corresponding author upon reasonable request.

REFERENCES

[1]J. Moser, J. Güttinger, A. Eichler, M. J. Esplandiu, D. Liu, M. Dykman, and A. Bachtold, Nat. Nanotechnol. **8**, 493 (2013).
[2]T. Nan, Y. Hui, M. Rinaldi, and N. X. Sun, Sci. Rep. **3**, 1985 (2013).
[3]M. S. Hanay, S. I. Kelber, C. D. O'Connell, P. Mulvaney, J. E. Sader, and M. L. Roukes, Nat. Nanotechnol. **10**, 339 (2015).
[4]M. Héritier, A. Eichler, Y. Pan, U. Grob, I. Shorubalko, M. D. Krass, Y. Tao, and C. L. Degen, Nano Lett. **18**, 1814 (2018).
[5]S. De Bonis, C. Urgell, W. Yang, C. Samanta, A. Noury, J. Vergara-Cruz, Q. Dong, Y. Jin, and A. Bachtold, Nano Lett. **18**, 5324 (2018).
[6]F. Fogliano, B. Besga, A. Reigue, L. Mercier de Lépinay, P. Heringlake, C. Gouriou, E. Eyraud, W. Wernsdorfer, B. Pigeau, and O. Arcizet, Nat. Commun. **12**, 4124 (2021).
[7]K. Ekinci, X. Huang, and M. Roukes, Appl. Phys. Lett. **84**, 4469 (2004).
[8]K. Ekinci, Y. T. Yang, and M. Roukes, J. Appl. Phys. **95**, 2682 (2004).
[9]H. Postma, I. Kozinsky, A. Husain, and M. Roukes, Appl. Phys. Lett. **86**, 223105 (2005).
[10]S. K. Roy, V. T. Sauer, J. N. Westwood-Bachman, A. Venkatasubramanian, and W. K. Hiebert, Science **360**, eaar5220 (2018).
[11]A. Demir and M. S. Hanay, IEEE Sens. J. **20**, 1947 (2019).
[12]Y. Martin, C. C. Williams, and H. K. Wickramasinghe, J. Appl. Phys. **61**, 4723 (1987).
[13]H. Gress, J. Barbish, C. Yanik, I. Kaya, R. Erdogan, M. Hanay, M. González, O. Svitelskiy, M. Paul, and K. Ekinci, Phys. Rev. Appl. **20**, 044061 (2023).
[14]A. Husain, J. Hone, H. W. C. Postma, X. Huang, T. Drake, M. Barbic, A. Scherer, and M. Roukes, Appl. Phys. Lett. **83**, 1240 (2003).
[15]M. M. Parmar, P. Gangavarapu, and A. Naik, Appl. Phys. Lett. **107**, 113108 (2015).
[16]J. Molina, J. E. Escobar, D. Ramos, E. Gil-Santos, J. J. Ruz, J. Tamayo, Á. San Paulo, and M. Calleja, Nano Lett. **21**, 6617 (2021).
[17]I. Kozinsky, H. Postma, I. Bargatin, and M. Roukes, Appl. Phys. Lett. **88**, 253101 (2006).
[18]H. Cho, M.-F. Yu, A. F. Vakakis, L. A. Bergman, and D. M. McFarland, Nano Lett. **10**, 1793 (2010).
[19]J. Gieseler, L. Novotny, and R. Quidant, Nat. Phys. **9**, 806 (2013).
[20]A. W. Barnard, M. Zhang, G. S. Wiederhecker, M. Lipson, and P. L. McEuen, Nature **566**, 89 (2019).
[21]I. Kozinsky, H. C. Postma, O. Kogan, A. Husain, and M. L. Roukes, Phys. Rev. Lett. **99**, 207201 (2007).
[22]J. S. Huber, G. Rastelli, M. J. Seitner, J. Kölbl, W. Belzig, M. I. Dykman, and E. M. Weig, Phys. Rev. X **10**, 021066 (2020).
[23]R. Lifshitz and M. C. Cross, *Nonlinear Dynamics of Nanomechanical and Micromechanical Resonators* (Wiley Online Library, 2008).
[24]A. H. Nayfeh and D. T. Mook, *Nonlinear Oscillations* (John Wiley & Sons, 2008).
[25]L. D. Landau and E. M. Lifshitz, *Course of Theoretical Physics* (Elsevier, 2013).
[26]A. Bachtold, J. Moser, and M. Dykman, Rev. Mod. Phys. **94**, 045005 (2022).
[27]J. S. Ochs, G. Rastelli, M. Seitner, M. I. Dykman, and E. M. Weig, Phys. Rev. B **104**, 155434 (2021).
[28]A. Keskekler, H. Arjmandi-Tash, P. G. Steeneken, and F. Alijani, Nano Lett. **22**, 6048 (2022).
[29]M. I. Younis and A. Nayfeh, Nonlinear Dyn. **31**, 91 (2003).
[30]K. Moskovtsev and M. Dykman, Phys. Rev. B **95**, 085426 (2017).
[31]C. Samanta, N. Arora, and A. Naik, Appl. Phys. Lett. **113**, 113101 (2018).
[32]A. Castellanos-Gomez, R. van Leeuwen, M. Buscema, H. S. van der Zant, G. A. Steele, and W. J. Venstra, Adv. Mater. **25**, 6719 (2013).
[33]A. Hajjaj, F. Alfosail, and M. I. Younis, Int. J. Nonlinear Mech. **107**, 64 (2018).
[34]J. S. Ochs, D. K. Boneß, G. Rastelli, M. Seitner, W. Belzig, M. I. Dykman, and E. M. Weig, Phys. Rev. X **12**, 041019 (2022).
[35]R. T. Erdogan, M. Alkhaled, B. E. Kaynak, H. Alhmoud, H. S. Pisheh, M. Kelleci, I. Karakurt, C. Yanik, Z. B. Sen, B. Sari *et al.*, ACS Nano **16**, 3821 (2022).
[36]O. Malvar, J. Ruz, P. M. Kosaka, C. M. Domínguez, E. Gil-Santos, M. Calleja, and J. Tamayo, Nat. Commun. **7**, 13452 (2016).
[37]P. Truitt, J. Hertzberg, E. Altunkaya, and K. Schwab, J. Appl. Phys. **114**, 114307 (2013).
[38]O. Maillet, X. Zhou, R. R. Gazizulin, R. Ilic, J. M. Parpia, O. Bourgeois, A. D. Fefferman, and E. Collin, ACS Nano **12**, 5753 (2018).
[39]I. Kozinsky, "Nonlinear nanoelectromechanical systems," Ph.D. thesis (California Institute of Technology, 2007).
[40]J. Barbish, C. Ti, K. Ekinci, and M. Paul, J. Appl. Phys. **132**, 034501 (2022).
[41]A. B. Ari, M. S. Hanay, M. R. Paul, and K. L. Ekinci, Nano Lett. **21**, 375 (2020).
[42]B. Hauer, C. Doolin, K. Beach, and J. Davis, Ann. Phys. **339**, 181 (2013).
[43]C. Ti, J. McDaniel, A. Liem, H. Gress, M. Ma, S. Kyoung, O. Svitelskiy, C. Yanik, I. Kaya, M. Hanay *et al.*, Appl. Phys. Lett. **121**, 023506 (2022).
[44]M. Ma and K. L. Ekinci, J. Appl. Phys. **134**, 074302 (2023).

[45]C. Ti, A. B. Ari, M. C. Karakan, C. Yanik, I. I. Kaya, M. S. Hanay, O. Svitelskiy, M. González, H. Seren, and K. L. Ekinci, Nano Lett. **21**, 6533 (2021).
[46]L. G. Villanueva and S. Schmid, Phys. Rev. Lett. **113**, 227201 (2014).
[47]Y. S. Klaß, J. Doster, M. Bückle, R. Braive, and E. M. Weig, Appl. Phys. Lett. **121**, 083501 (2022).
[48]Q. P. Unterreithmeier, T. Faust, and J. P. Kotthaus, Phys. Rev. Lett. **105**, 027205 (2010).
[49]M. Cross and R. Lifshitz, Phys. Rev. B **64**, 085324 (2001).
[50]P.-L. Yu, T. Purdy, and C. Regal, Phys. Rev. Lett. **108**, 083603 (2012).
[51]S. A. Fedorov, N. J. Engelsen, A. H. Ghadimi, M. J. Bereyhi, R. Schilling, D. J. Wilson, and T. J. Kippenberg, Phys. Rev. B **99**, 054107 (2019).
[52]I. Bargatin, I. Kozinsky, and M. Roukes, Appl. Phys. Lett. **90**, 093116 (2007).
[53]V. Kara, V. Yakhot, and K. L. Ekinci, Phys. Rev. Lett. **118**, 074505 (2017).